Editors' Suggestion

Integrated Hybrid Plasmonic-Photonic Device for All-Optical Switching and Reading of Spintronic Memory

Hamed Pezeshki,[1,2,3,*] Pingzhi Li,[1] Reinoud Lavrijsen,[1,2] Martijn Heck,[2] Erwin Bente,[2] Jos van der Tol,[2] and Bert Koopmans[1,2]

[1] *Department of Applied Physics and Science Education, Eindhoven University of Technology, 5612 AZ Eindhoven, Netherlands*
[2] *Eindhoven Hendrik Casimir Institute, Center for Photonic Integration, Eindhoven University of Technology, 5600 MB Eindhoven, Netherlands*
[3] *EFFECT Photonics B.V., 5616 LZ Eindhoven, Netherlands*

(Received 25 January 2023; revised 10 March 2023; accepted 31 March 2023; published 10 May 2023)

We introduce a hybrid plasmonic-photonic device for on-chip all-optical switching and reading of ferrimagnet bits with perpendicular magnetic anisotropy in a racetrack spintronic memory, coupled onto an indium phosphide waveguide. The device comprises V-shaped gold plasmonic nanoantennas coupled with a photonic crystal cavity, which enables switching and reading of the magnetic state of nanoscale bits by enhancing the absorbed energy density and polar magneto-optical Kerr effect locally. Using a finite-difference time-domain method, we show that our device can switch and read targeted bits down to 100 nm in the presence of oppositely magnetized background regions in the racetrack with widths up to 120 nm, clearly outperforming a bare photonic waveguide. Our hybrid device provides the missing link between integrated photonics and nanoscale spintronics by tackling the challenges of nonlinear absorption in the waveguide, weak magneto-optics, and size mismatch, leading to the development of ultrafast and energy-efficient advanced on-chip applications.

DOI: 10.1103/PhysRevApplied.19.054036

I. INTRODUCTION

The fields of integrated photonics and spintronics have been identified as two of the fastest-growing directions for the new generation of solid-state application platforms. Integrated photonic platforms, such as the silicon (Si)-on-insulator (SOI) [1,2] and the indium phosphide (InP) membrane on Si (IMOS) [3,4], enable high-bandwidth and energy-efficient data transmission, and have achieved great maturity over the years. In the meantime, spintronics promises the development of fast, energy-efficient, ultrafast and ultradense data memory devices [5]. Much progress has already been made in the areas of magnetic random access memory (MRAM) [5] with sizable commercialization. Meanwhile, a racetrack memory [6], in which trains of magnetic bits in magnetic nanoconduits are controlled by employing cutting-edge spintronic effects, has been proposed to further upgrade the low-level cache in terms of speed, areal density and energy consumption [7,8]. Logically, it can be envisioned that further gains in speed and energy efficiency can be achieved by merging photonics and spintronics domains into a single platform [9]. Nevertheless, such a hybrid integration is not yet available since the communication between the two domains has to be controlled via the electronics acting as an intermediate domain, which creates power/time/area overhead, compromising the potential advantage of the hybrid integration. A possible way to mitigate this issue is the direct access (switching and reading) of spintronic memory by photonics.

So far, all-optical reading (AOR) of a magnetic material exploiting the polar magneto-optical (MO) Kerr effect (PMOKE), that is, the magnetization-dependent variation in the polarization state of light reflected off the surface of a magnetic material, has been used as a standard method of reading a standalone magnetic bit in the absence of oppositely magnetized neighboring bits [10–13]. Recently, all-optical switching (AOS) [14–17] was shown to be a next step forward for optical access of the magnetic information from the fast-advancing spintronic memory platforms [5,9]. Recent advancements in AOS were embodied in the discovery of single-pulse AOS in more process-compatible synthetic ferrimagnets, such as cobalt (Co)/gadolinium (Gd) [17] and [Co/terbium (Tb)]$_m$ [18,19] multilayered material platforms, having m repetition(s). This approach provides low switching energy [20] and is compatible with integration to state-of-the-art spintronic building blocks [19,21–24].

Nevertheless, coupling light energy directly to spintronic devices comes with the obvious drawback of inefficient

*h.pezeshki@tue.nl; hamedpezeshki@effectphotonics.com

interaction due to the large size mismatch between the waveguide mode and the size of spintronic devices [5], as a result of the diffraction limit. Such an issue not only offsets the energy efficiency of AOS but also imposes challenges on the scalability of such hybrid integration. Moreover, the large transient power needed for AOS can incur additional losses in the waveguide due to nonlinear absorption [23]. Similar issues also persist for AOR as weak coupling limits the MO interaction, resulting in a small PMOKE, even at large footprints. Therefore, a photonic design to focus light beyond the diffraction limit, while ensuring efficient energy transfer, is required. Here, we propose the concept of a hybrid plasmonic nanoantenna (PNA) and photonic crystal (PhC) cavity to curb the above-mentioned challenges.

Noble metal nanostructures such as gold PNAs can strengthen the light-matter interaction beyond the diffraction limit by localizing and enhancing incident electromagnetic energy in nanoscale spots at the metal interface using localized surface plasmon resonance (LSPR) [25,26]. The magnified light-matter interaction enables PNAs to enhance the scattering and absorption cross sections of coupled nanoparticles, improving their effective polarizability and absorbed energy density. Such characteristics have turned PNAs into key components in designing miniaturized photonic devices in a variety of applications, ranging from telecoms [27,28] to biosensing [29,30]. Therefore, it is expected that PNAs can likewise play a key role in enhancing the MO activity at the nanoscale and consequently addressing the scalability issue.

Despite large enhancement of the electric field provided by a PNA, the interaction cross section is still limited due to its small feature size. We propose the use of a PhC cavity [31–33] to further improve the interaction cross section. A PhC cavity, basically a Bragg grating cavity based on periodic dielectric structures satisfying the Bragg condition [34,35], provides high spatial light confinement in a diffraction-limited cavity. The confined light in the cavity enhances the effective light-matter interaction cross section, making PhC cavities attractive for various applications such as lasing and optical switching [36–38].

With the above notions, we thus introduce the design of a hybrid PNA-PhC device coupled with a magnetic racetrack [8,39,40] to bring all the advantages of both concepts in one place for performing enhanced AOS and PMOKE-based AOR of ferrimagnetic bits with perpendicular magnetic anisotropy (PMA) on a photonic integrated platform [Fig. 1(a)]. Such a compact device allows for a direct energy-efficient transport of information from the spintronic domain to the photonic domain without the need for intermediate electronics for signal conversion. Our hybrid device, which consists of a double V-shaped gold PNA coupled to a PhC cavity, can provide the threshold light fluence for AOS of Co/Gd magnetic films [8,17,20]

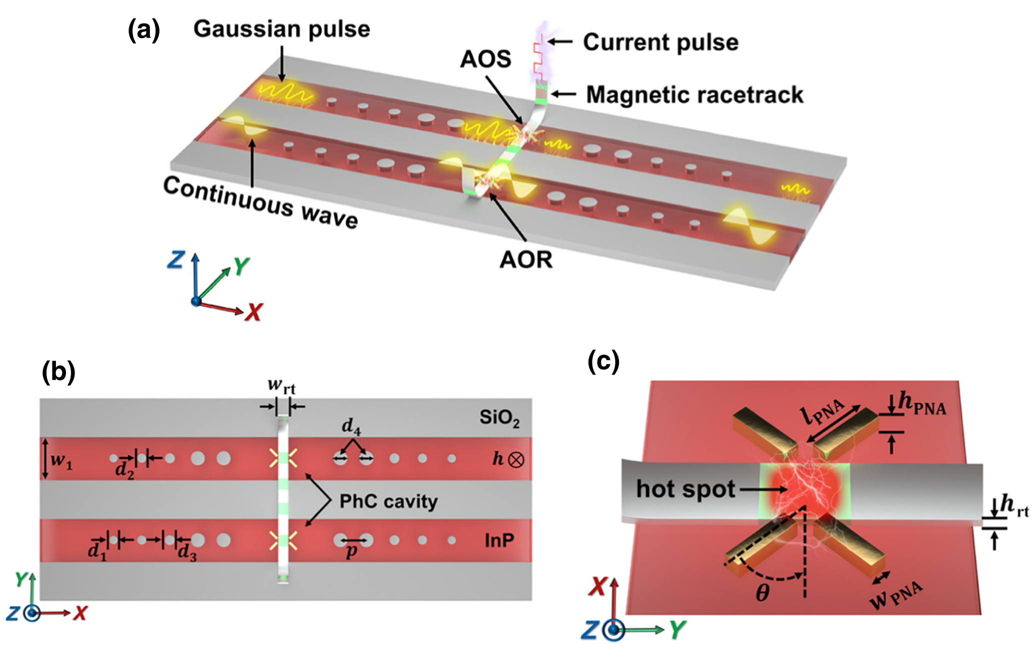

FIG. 1. Conceptual illustration of the hybrid all-optical switching/reading (AOS/AOR) device. (a) Perspective view showing how the proposed device functions. (b) Top view of the platform presenting design parameters of the photonic crystal (PhC) cavity, $d_{1-4} =$ 100, 110, 120, and 170 nm are the holes diameters with a pitch, p, of 370 nm. The waveguides have a width and a height of $w_1 = 570$ nm and $h = 280$ nm, while the magnetic racetrack width, w_{rt}, is 120 nm. (c) Magnified view of the plasmonic nanoantenna (PNA) and the racetrack, where the length, height and width of the PNA elements are $l_{PNA} = 120$ nm, $h_{PNA} = w_{PNA} = 30$ nm, and they are oriented at an angle of $\theta = 45^{\circ}$ with reference to the waveguide direction. The racetrack height, h_{rt}, is 10 nm.

and improve the inherently weak PMOKE for AOR by efficiently focusing light onto a nanoscale spot in a magnetic racetrack using LSPR. Note that our Co/Gd- based magnetic racetrack encodes information as domains with “up” and “down” magnetization states in a magnetic racetrack. These domains can be coherently moved at high velocity (faster than 1 km/s) [8] by a combination of spin-orbit torque [41] and Dzyaloshinskii-Moriya interaction [7,42] driven domain wall motion exerted by electrical current [40]. We stress that our choice for PMA thin films is motivated by its leading role in state-of-the-art spintronics.

We use three dimensional finite-difference time-domain (FDTD) method [43] on devices designed in the IMOS platform. We show that using our hybrid device, for an incident optical pulse energy of 0.6 pJ, the magnified absorbed energy density in the racetrack memory can be large enough to provide a switching fluence of 0.5 mJ/cm^2 for switching magnetic bits with sizes of down to about 100 nm in a racetrack with a width of 120 nm. By reducing the racetrack’s width down to 30 nm, further enhancement of the light-matter interaction increases the absorbed energy density in the racetrack such that switching of the magnetization in magnetic bits down to about 60 nm can be realized for an ultralow incident pulse energy of 0.15 pJ. Moreover, our hybrid device enables the optical detection of magnetization in targeted bits down to about 100 nm in a racetrack with widths of 30–120 nm, regardless of the magnetization in the rest of the racetrack. Although simulations were performed for IMOS, our model utilizes generic concepts that can be implemented in other popular photonic platforms such as SOI [1] and silicon nitride [44]. We believe this device can be a significant step toward addressing the fundamental issue of hybrid spintronic-photonic integration imposed by the light diffraction limit and inefficient coupling, allowing the creation of new generation on-chip and interchip applications.

II. DESIGN CONSIDERATIONS

Within the scope of this work, we explore the MO interaction between the light in an InP waveguide in a standard IMOS platform and a magnetic racetrack as a top cladding of the waveguide coupled to a hybrid PNA-PhC. The platform concept is schematically depicted in Fig. 1. It consists of two parallel InP waveguides with silica (SiO_2) side walls, where a racetrack is coupled orthogonally on top of the waveguides. For the occurrence of single-pulse AOS in process-compatible metallic magnetic structures, a combination of a (3d) transition metal ferromagnet and a (4f) rare-earth ferromagnet is essential [9,14,45]. For this reason, the racetrack consists of a multilayer stack of (from bottom to top) a 4-nm heavy metal seed layer, a 2-nm ferromagnetic Co layer, and a 4-nm Gd layer (see Appendix A 1). A Gaussian pulse (for AOS) and a continuous wave (for AOR) both with a free space wavelength of 1.55 μm (in the telecom C-band), are coupled into the transverse electric (TE_0) mode of both waveguides. The propagating light mode in the waveguide couples to the PhC cavity, where the light mode is spatially confined and enhanced at the center of the cavity. The spatially enhanced mode then evanescently excites the PNA by which light gets further focused and enhanced in a nanospot at the central gap of the PNA. The concentrated and enhanced light energy interacts with the racetrack locally and a domain at the nanospot is thermally switched [17,45,46]. By injecting current pulses through the racetrack [see Fig. 1(a)], the switched ferrimagnetic bit at the nanospot of the racetrack on top of the waveguide is moved along the racetrack toward the bottom waveguide, where it can be read out by the enhanced PMOKE in the nanospot at the central gap of the PNA. Such a monolithic integration scheme gives room to the fabrication of spintronic building blocks directly in the existing platform, interfacing to both integrated photonics and complementary metal-oxide-semiconductor (CMOS) without requirements for a complex interchip integration.

The design parameters are indicated in Figs. 1(b) and 1(c). The width and height of the racetrack are $w_{rt} =$ 120 nm and $h_{rt} = 10$ nm, the width and height of the waveguides are $w_1 = 570$ nm and $h = 280$ nm (see Supplemental Material 1 [47] for the design principle). The PhC cavity is designed by removing the central three holes from the PhC structure to create a resonant cavity at a wavelength of 1.55 μm (see Supplemental Material 2 [47]). The holes toward the end of the PhC cavity are tapered down to lower the backreflection by providing an impedance match between the waveguide mode and cavity mode. The pitch, p, is 370 nm and the holes diameters are $d_1 = 100$ nm, $d_2 = 110$ nm, $d_3 = 120$ nm, and $d_4 = 170$ nm. The PNA, which is composed of two coupled V-shaped gold nanoantennas, has a length, width, and height of $l_{PNA} = 120$ nm and $w_{PNA} = h_{PNA} = 30$ nm respectively, and the PNA elements are oriented at an angle of $\theta = 45^\circ$ with reference to the waveguide direction. The PNA has a resonance peak at 1.55 μm to optimize the light-matter interaction (see Supplemental Material 3 [47]).

Next, in order to validate the above-mentioned design in the sections below, we discuss the considerations regarding the power/energy limitation in a semiconductor waveguide, taking the example of an InP waveguide, as imposed by the known nonlinear effects.

A. Energy considerations for all-optical switching

AOS is considered the least dissipative and the fastest form of magnetization switching [9]. It is accomplished by ultrafast excitation (heating) of free electrons by a light pulse and subsequent angular momentum transfer between two sublattices (Co and Gd in our case) [9,45,46,48]. Nevertheless, the necessity of heating the metal nonadiabatically up to the Curie temperature point within a pulse duration [14,15,45] requires short pulses with a significant peak power. As a consequence, nonlinear losses, particularly, two- photon absorption (TPA) and free-carrier absorption (FCA) [49–51], in a semiconductor photonic waveguide (e.g., made of Si and InP) might be incurred. Observations have been made previously both in IMOS [49] and SOI [23] platforms, both showing significant nonlinear losses as the peak power of the pulses surpasses 0.1 W.

Previous works on AOS [14,17,20,52,53] have demonstrated that an absorbed fluence threshold of around 0.5 $\mathrm{mJ/cm^2}$ is needed for switching a domain in a Co/Gd bilayer spintronic material stack. This fluence corresponds to an energy deposition of 13 fJ to a waveguide's cladding with an area of $50 \times 50\ \mathrm{nm^2}$ for a pulse shorter than 500 fs, which accounts for a peak power density of at least 1 $\mathrm{GW/cm^2}$. Such a peak power density is close to the photon density that induces nonlinear losses [54]. Due to the finite coupling efficiency between light in the waveguide and spintronic cladding as well as a limited interaction cross section, the incident peak power density essential for switching is expected to be even larger. Fortunately, earlier works [52,55] showed successful AOS with a much longer pulse, around 10 ps, where the threshold energy for AOS has not been increased by more than a factor of 2. Therefore, to get an idea of the power/energy limitation (due to nonlinear absorption) in a waveguide in the IMOS platform based on earlier studies is of paramount importance for device design.

Here, we based our theoretical study on the traveling wave circuit model using the in-house PHIsim modeling software [56], with the extension of nonlinear effects (see Appendix A 2). We further note that the TPA coefficient is the essential parameter for the TPA-induced nonlinear losses; it is chosen to be 1.5×10^{-10} m/W, the value characterized for the IMOS platform [49,51,57]. On the other hand, the free carrier lifetime is a key parameter for FCA-induced losses. However, there is a large discrepancy between values reported so far for InP based structures (from 1 ps–1000 ps) [50,58,59]. Nevertheless, we found that FCA contributes negligibly (less than 5%) to the total nonlinear losses, even for the value of 2000 ps. We therefore chose the free carrier lifetime to be a conservative value of 2000 ps (the higher the lifetime, the larger the loss), which is believed not to affect the validity of our result.

In our model we investigated the energy transmission of a Gaussian optical pulse having a $\mathrm{TE_0}$ mode profile with various pulse energies in a standard IMOS passive waveguide with a length of 1 mm, which corresponds to a reasonable dimension estimated for the length of supporting photonic distribution networks for AOS. We also considered different pulse durations in our simulation, keeping values within the margins for successful AOS [52,55]. The physical parameters involved are taken from both the available literature as well as our simulation results from the MODE solver [60].

As for discussing the generic insight, we first neglect the passive loss of the waveguide. Figure 2(a) shows the transmission through the waveguide in which a "cut-off" behavior can be seen as the energy ramps up over a threshold energy. Such a threshold energy is almost 100 times higher for a 10^4-fs pulse than a 100-fs one, due to the fact that the "cut-off" threshold is limited by the peak power. In other words, the output energy will saturate over a certain input energy level. This suggests that in order to ensure

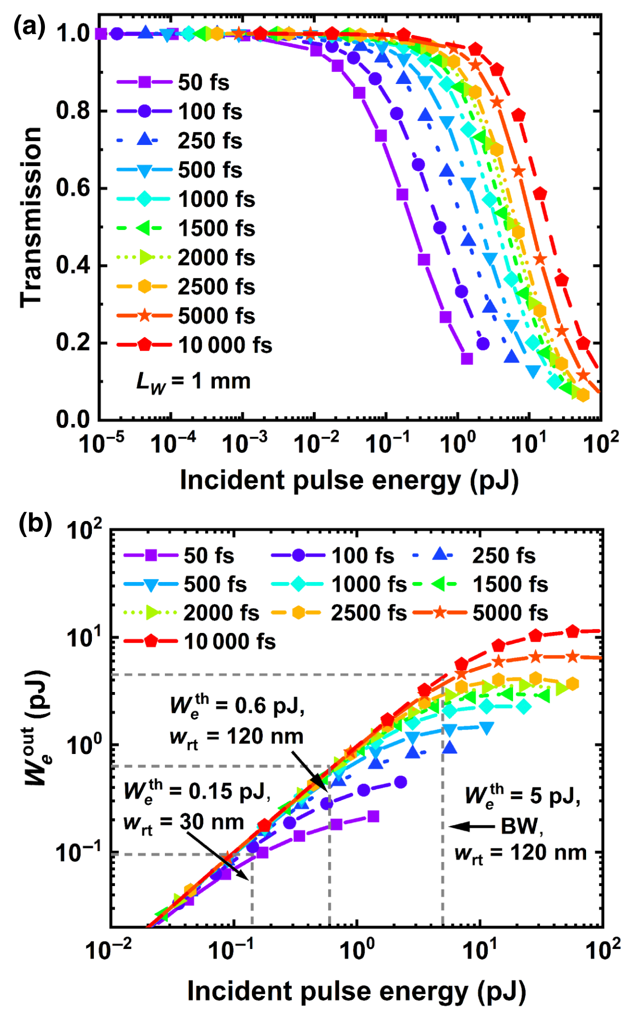

FIG. 2. Numerical investigation of the impact of nonlinear absorption on AOS in the IMOS platform using the PHIsim modeling software [56]. (a),(b) Transmission of an optical pulse and an output energy, W_e^{out}, in terms of an incident pulse energy for various pulse durations through a 1-mm-long waveguide. The gray dashed lines in (b) relate the threshold incident input pulse energies (W_e^{th}) and their corresponding output energies, W_e^{out}, for three different cases of the bare waveguide (BW) for a racetrack width of $w_{rt} = 120$ nm and the hybrid device with $w_{rt} = 120$ nm and 30 nm.

the power efficiency for AOS and avoid possible heat dissipation due to nonlinear absorption, the incident pulse energy needs to be kept below 15 pJ for a 10 ps pulse [see Figs. 2(a) and 2(b)]. As for short pulses (below 500 fs), such a requirement is limited to less than 1 pJ. The output pulse energy (W_e^{out}) with consideration of a typical passive loss of 3.5 dB/cm for an InP waveguide in the IMOS platform is plotted in Fig. 2(b). Results show that the output energy remains linear relative to the input energy up to the "cut-off" energy point. Based on this figure, one needs to stay in the linear regime shown in Fig. 2(b) to have negligible TPA and FCA, and, for 10 ps, this means the maximum deliverable energy of around 4.5 pJ for 5 pJ sent in, for a photonic network of 1 mm. Of course, this is just an example and Fig. 2(b) will serve as a benchmark in this paper.

III. RESULTS

A. All-optical switching

As AOS is a heat-driven process [14,45], we assess it in our numerical study using FDTD [43] based on the instantaneous absorbed energy density of the magnetic racetrack on top of the waveguide. In our simulation, we extract the spatial distribution of the absorbed energy by the racetrack, which is then compared with an experimentally characterized threshold fluence of 0.5 $\mathrm{mJ/cm^2}$ to determine the presence of AOS. The optimal PNA-PhC device was presented in Fig. 1. Nonetheless, to show our design protocol for reaching our optimized configuration, we present the results progressively for case studies of five configurations involving the intermediate steps, each of which was optimized, individually.

Figure 3(a) shows the five configurations along side their corresponding two-dimensional electric field distribution across the waveguide in the X-Y plane. We start by examining the case of the bare waveguide (BW) as shown in panel I, where no other photonic component is present. In this case, the light interaction with the spintronic material is limited due to the diffraction limit, which can be evidenced by the field distribution showing almost no modification of the incident light after passing through the racetrack. As a result of the insignificant light-matter interaction, around 90% of the propagating light is delivered to the waveguide's output. We further calculated the absorbed energy density in the racetrack and plotted the results along the Y axis by averaging the value along the X and Z axes within the region of the racetrack right on top of the waveguide as shown in Fig. 3(b), where the peak energy density for the case of BW is normalized to 1. The nearly flat absorption profile [see the purple curve in Fig. 3(b)] shows the large footprint of the switching region, which almost fits the width of the waveguide. In order to exceed the energy threshold of 0.5 $\mathrm{mJ/cm^2}$ [20] for AOS, we found that an incident threshold pulse energy of at least $W_e^{\mathrm{th}} = 5$ pJ is required in this case. This amount of incident pulse energy is found to be unacceptable (let alone the large switching footprint) as indicated by the results shown in Fig. 2(b); see the rightmost gray dashed line, which shows nonlinear absorption loss of $(W_e^{\mathrm{th}} - W_e^{\mathrm{out}})/(W_e^{\mathrm{th}}) \geq$ 16% for a pulse duration of 10 ps propagating over 1 mm, caused by TPA and FCA. For a pulse durations shorter than 5 ps, such a value cannot be delivered. Considering the initial result, a certain photonic design is needed to enhance the absorbed energy density of the racetrack and to minimize nonlinear absorption loss as well as to reduce the footprint of switching.

For the second configuration, we coupled the racetrack with a PNA as shown in panel II of Fig. 3(a). Based on the electric field distribution in this panel, a slight enhancement in the light-matter interaction can be seen, which resulted in a reduced waveguide transmission of 75%. However, this enhanced interaction is not sufficient to provide enough energy for AOS such that, according to Fig. 3(b), the maximum absorbed energy by the racetrack is enhanced only from 1% to 1.9%. To further enhance the absorption cross section of the racetrack, we created a configuration based on a one- dimensional periodic array of PNAs [panel III in Fig. 3(a)]. By making an array of PNAs with a certain pitch, plasmonic surface lattice resonance is excited via coupling LSPR of each PNA together [61,62]. The resultant lattice resonance can further increase the localized electric field and enhance the absorbed energy density of a nanoparticle coupled to the PNA array. The light transmission in this case drops from 75% to about 48%, implying further enhancement in the interaction between the propagating light, PNA array, and racetrack. By looking at Fig. 3(b), we see a pronounced spike in the absorbed energy density having a maximum enhancement of 3.2× with a full width at half maximum (FWHM) of about 140 nm. Despite the drop in the transmission for the case of the PNA array, we see that the absorbed energy density of the racetrack did not increase significantly. Addition of more PNA elements in the array did not improve the result due to the lossy nature of gold [63].

Based on the results so far, we looked for alternative approaches to find a solution that brings further enhancement in the energy absorption by the racetrack. As mentioned in Sec. I, a PhC cavity is a photonic component that can enhance the electric field by spatial confinement of light. So we designed a configuration based on a PhC cavity as schematically presented at the left side of panel IV in Fig. 3(a). The field distribution plot at the right side of this panel clearly shows the appearance of the cavity mode from which the electric field enhancement of 2.5× in the middle of the waveguide is achieved. For this configuration, the light transmission is around 54%. For the design of the cavity, careful attention was paid to the reflectivity, which is only around 8% and makes such a design highly energy-efficient. The reflection was lowered by reducing the number of holes as well as tapering down the radii of the holes toward the end sides of this cavity to reduce the mismatch between the waveguide and cavity modes as much as possible, while keeping the electric field enhancement reasonably high [see panel IV in Fig. 3(a)]. According to Fig. 3(b), introducing the configuration with the PhC cavity is promising in that the absorbed energy density shows an enhancement of 1.6× relative to the PNA array configuration, that is, the peak absorbed energy density rises from 3.2 to 5, while in general it shows 5× enhancement relative to the BW configuration [see Fig. 3(b)]. However, the drawback of this configuration is its broad absorption profile (with an FWHM of about 260 nm) across the racetrack, which originates from the physical issue that a PhC cavity cannot overcome the diffraction limit of light. Upon increasing the incident pulse energy, the broad absorption profile of this configuration can increase the probability of the occurrence of TPA and FCA at the center of the cavity, which consequently can prohibit AOS from happening.

In order to take advantage of the higher power absorption enhancement of the PhC configuration and the narrower FWHM of the PNA one, we propose the hybrid scheme in which a PNA is coupled at the center of the PhC cavity as shown in panel V of Fig. 3(a). The reason for using one PNA instead of an array is to avoid additional light loss in the system by the extra PNA elements constituting the array. Using this configuration, the light transmission decreases further from 54% to 43%, while the reflection is as small as 12%. Based on Fig. 3(b), the hybrid PNA-PhC configuration resulted in a maximum 7×

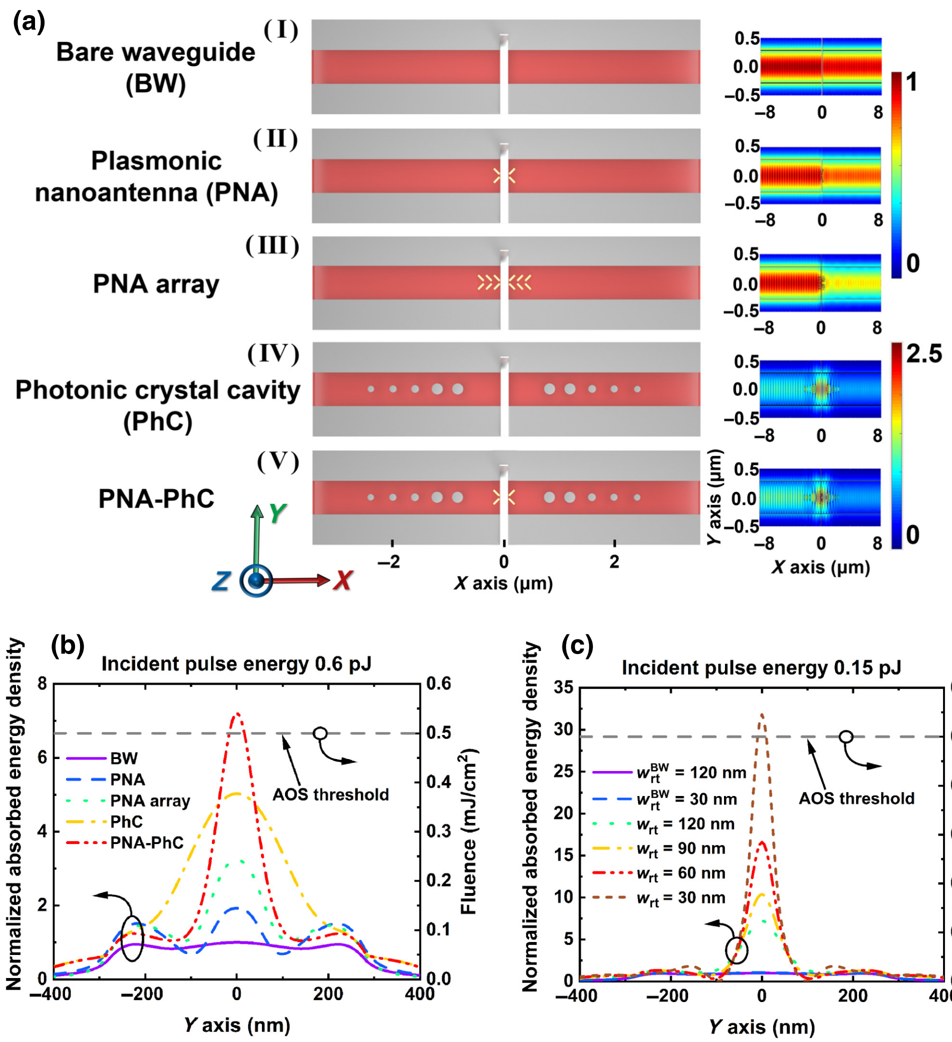

FIG. 3. Illustration of AOS. (a) Schematic diagram of five different configurations alongside their correspondent electric field distributions in the X-Y plane through the waveguide. Normalized absorbed energy density and the projected fluence, averaged along the width and thickness of the racetrack for: (b) five different configurations, and (c) the PNA-PhC device (V) with racetrack widths (w_{rt}) of 30 to 120 nm as well as the BW device (I) with w_{rt} of 120 and 30 nm, respectively.

enhancement in the absorbed energy density compared to the initial BW configuration. More importantly, using this configuration, the maximum amount of power absorbed by the racetrack is high enough such that for an incident pulse energy of 0.6 pJ, we reached the threshold fluence of 0.5 mJ/cm^2 for AOS. Referring back to Fig. 2(b) shows that for an input power of 0.6 pJ, the relation between the output and input energies is in the linear regime, which implies that the probability of the occurrence of TPA and FCA is significantly suppressed.

With advancements in spintronic applications, an MRAM size down to below 100 nm with a robust operation has long been demonstrated [5]. Moreover, the interfacial anisotropy (greater than 0.5 MJ/m^2) in Pt/Co/Gd [21,22,64] is expected to be enough to support thermally stable sub-100-nm domains. It is a known fact that scaling down the MRAM and racetrack brings further energy/speed gain [40,65]. Hence, we inspected the impact of scaling down the racetrack's width, w_{rt}, on the AOS performance with the PNA-PhC device. Here, we keep a fixed distance between the edge of the racetrack and PNA. The absorbed energy density is plotted for w_{rt} of 120, 90, 60, and 30 nm in Fig. 3(c). For comparison purposes, the results for the BW configuration with a w_{rt} of 120 and 30 nm are also plotted. The hybrid device with $w_{\mathrm{rt}} = 30$ nm achieved more than 30× enhancement compared to the BW one with w_{rt} of 120 and 30 nm. This enhancement is related to the stronger light-matter interaction due to the reduced distance between the PNA elements. More interestingly, for such a large enhancement of the absorbed energy density by the hybrid device at $w_{\mathrm{rt}} = 30$ nm, the threshold fluence can be reached for an incident pulse energy as small as 0.15 pJ. Furthermore, by looking at Fig. 2(b), one can see that for pulse lengths of 50 to 10^4 fs, the system's response for a 0.15 pJ input pulse energy is linear, pointing to the absence of the TPA and FCA phenomena in the device. Moreover, the absorbed energy density was found to have an FWHM of about 60 nm, much smaller than the conventional optics are able to focus. Therefore, our results elucidate the capability of the hybrid design in optically addressing sub-100-nm spintronic devices, compatible for high-density data packing.

B. All-optical reading

So far, we have shown the possibility of on-chip AOS in an area/energy-efficient fashion with the help of the combined efforts of both PNA and PhC. Similarly, MO interactions can be enhanced using the hybrid device. Following switching a magnetic state, the magnetic information can be read out on the same photonic chip using PMOKE by which information can be encoded in the photonic domain as an intensity variation of the transverse magnetic (TM_0) mode. We will evaluate the performance of AOR based on the magnitude of the PMOKE-induced polarization change (Kerr rotation) and the minimum bit size that can be distinguished independent of all other neighboring bits in the racetrack. In order to find the minimum bit size readable in the racetrack, we investigate the evolution of the Kerr rotation along the propagation direction of light through the waveguide in terms of the size of the target magnetic bit in the presence of the oppositely magnetized remainder of the racetrack. Then, from this information, we calculate the magnitude and phase of the Kerr rotation in terms of the target bit size to explore the minimum readable bit size.

Figure 4(a) shows the evolution of the Kerr rotation across the waveguide of the PNA-PhC device, Fig. 3(a), in terms of different domain widths (DWs) of the target magnetic bit. The target magnetic bit is shown in red, surrounded by the oppositely magnetized background in green as sketched in the inset. As light interacts with the magnetic racetrack, a rise in the polarization rotation (i.e., Kerr rotation) as a result of PMOKE can be seen. The waveguide medium induces birefringence between the TE_0 and the PMOKE-induced TM_0 components of light as it propagates through the waveguide, leading to a beating between the two components. As a result, the induced Kerr rotation will be superposed with the beating oscillation, which in turn leads to an oscillation in the Kerr rotation along the light propagation direction as shown in Fig. 4(a). Note that the small oscillation in the Kerr rotation before the magnetic racetrack originates from the light backreflected from the racetrack and PNA. According to Fig. 4(a), the oscillation of the Kerr rotation, θ_K, for DW = 60 nm, is out of phase relative to the case with larger DWs such that it is almost reversed by 180° relative to the larger DWs.

To elaborate on this phase reversal, it is worth pointing out that the Kerr rotation is the sum of the contributions from all magnetic regions (i.e., the target bit and the background regions). For small DWs, the MO response originates mostly from the oppositely magnetized background regions, based on which we cannot detect the magnetization state of the target bit. On the other hand, as the DW increases from 120 nm to 570 nm, the MO contribution from the target bit dominates the MO contributions from the oppositely magnetized background regions, which consequently makes the magnitude of the Kerr rotation of the target bit greater than the superposition of the Kerr rotations of the background regions. Therefore, the magnetization state of the target bit can be identified unambiguously. A slight phase shift between the cases is a consequence of the phase difference in the beating pattern between the TE_0 and PMOKE-induced TM_0 components. Thus, we used the magnitude and phase of the Kerr rotation to calculate the strength of the MO interaction and the minimum readable bit size.

We extracted both the magnitude and phase of the Kerr rotation for all five configurations with a w_{rt} of 120 nm [see Fig. 3(a)] as a function of DW, where the results are plotted in Fig. 4(b). By increasing the DW, there is a minimum

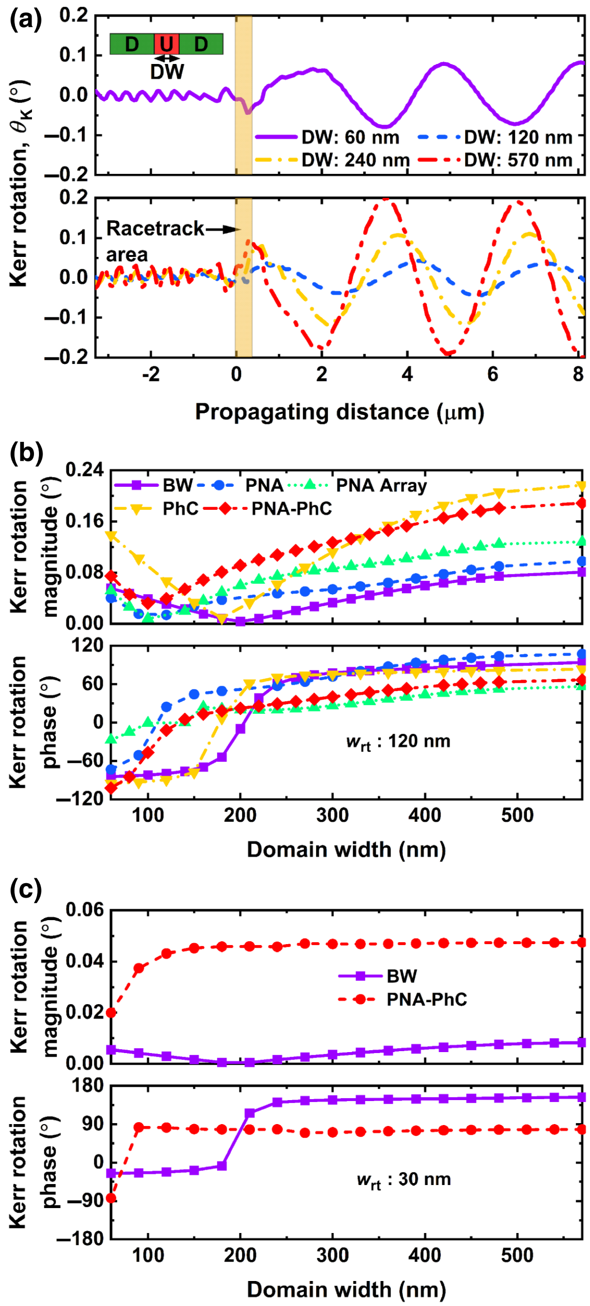

FIG. 4. Illustration of AOR. (a) The evolution of the Kerr rotation, θ_K, along the propagation direction inside the waveguide of the PNA-PhC device in terms of target magnetic bit widths of DW = 60, 120, 240, and 570 nm. The inset shows the target bit in red, surrounded by oppositely magnetized background in green. (b),(c) The Kerr rotation magnitude and phase in terms of the target DW for: (b) the five different configurations with a w_{rt} of 120 nm, and (c) the BW and PNA-PhC devices with a w_{rt} of 30 nm.

in the magnitude of the Kerr rotation which is accompanied by a sudden transition in the phase of the Kerr rotation in all devices. The minimum Kerr rotation happens at DW = 100 nm (200 nm) for the PNA-PhC (BW) device which comes with a jump in the state of the Kerr rotation phase as shown in Fig. 4(b). The minimum Kerr rotation magnitude and the jump in the phase are indeed due to the destructive interference between the individual Kerr rotations of the target bit and the oppositely magnetized neighboring bits in the racetrack. For very small DWs [e.g., DW $<$ 100 nm (200 nm) in the PNA-PhC (BW) device], the PMOKE response of the target bit is much smaller than the superposition of the PMOKE responses from the background regions with the opposite magnetization due to the limited MO contribution. Therefore, the resultant PMOKE response is determined predominantly by the magnetization in the rest of the racetrack. In contrast, with increasing DW [e.g., DW $>$ 100 nm (200 nm) in the PNA-PhC (BW) device], due to the continual enhancement of the MO contribution from the target bit, the PMOKE response from this bit gradually increases and dominates the PMOKE response from the superposition of the oppositely magnetized background bits. So the target magnetic bit with the "up" magnetization can be unambiguously determined above this value of DW, independent of the bit pattern in the background regions. Note that plasmonic effects distort the polarization state of light near the PNA more than regions apart. This perturbation leads to a phase difference between PMOKE responses from the targeted bit and the rest of the racetrack. The two contributions thus no longer exactly destructively interfere. That is why for PNA-based devices, the Kerr rotation magnitude does not go to zero.

The threshold DW above which the magnetization in the target bit can be detected is considered a measure for determining the resolution of the device. Based on Fig. 4(b), we can see that the PhC device improved the PMOKE response relative to the BW device, but it did not enhance the resolution due to the diffraction limit. However, the devices based on the PNA which benefit from LSPR increased the resolution by about 100 nm by enhancing the effective polarizability of the target bit in the subwavelength regime.

Finally, we compared the AOR performance of the BW and hybrid configurations for a w_{rt} of 30 nm to see the impact of shrinking the width of the racetrack on the AOR function. Based on Fig. 4(c), we can see that the detection resolution of the BW device does not change. In contrast, in the case of the hybrid device, due to the enhanced interaction between the PNA elements, the detection resolution reaches below 100 nm. Furthermore, by comparing the strength of the Kerr rotation in both cases, it is clear that the hybrid device has much better performance compared to the BW one, with roughly 5× enhancement for DWs greater than 100 nm. Overall, this subsection showed the possibility of determining the magnetization state in magnetic bits sizes of down to about 100 nm for the racetrack widths between w_{rt} = 30 and 120 nm, regardless of the magnetization state in the rest of the racetrack, using the hybrid PNA-PhC device.

C. Detection of the magnetization state

Reversing the magnetization state inverts the rotation angle of the polarization of the TE_0 component due to PMOKE. Consequently, this reversal in the rotation angle makes the phase of the PMOKE-induced TM_0 component relative to the TE_0 component change by 180°. To be able to detect this phase variation, a necessary next step is to convert such a response into a reading signal. In this subsection, we adopt the method proposed by Demirer *et al.* to convert this phase change to an intensity variation of the TM_0 component [12,13].

Here, we introduce a polarization converter (PC) based on an integrated plasmonic quarter-wave plate (QWP) [66] as an essential building block for such a conversion. Compared to conventional PCs based on slanted waveguides [12,13,67], a plasmonic PC has a higher fabrication process tolerance and we can tune the device performance by easily adjusting its geometrical parameters [68].

As the wave propagates through the PC, the phase difference can be translated into an intensity variation because of the partial conversion of the TE_0 component to the TM_0 component, where the intensity variation can be detected using an on-chip photodetector. The schematic of the PC is depicted in Fig. 5(a) in which, for the sake of clarity, the surrounding SiO_2 material is omitted. A gold metal layer with a thickness of 30 nm is coupled onto the InP waveguide with a width of $w_2 = 440$ nm. The length of the PC is $l_{PC} = 1860$ nm, while its width is $w_{PC} = 180$ nm. To avoid excessive absorption loss caused by the gold, a SiO_2 spacer layer with a thickness of 20 nm, so $h_{PC} = 50$ nm, and with the same length is introduced between the InP waveguide and the gold thin film. It is important to note that the dimensions of the proposed PC and the width of the waveguide are optimized to create efficient QWP functionality, that is, rotating the eigenstates by 45° and making the difference in the magnitude of the TE_0 and TM_0 components approach zero [69].

To elaborate on the process of translating the phase change to the intensity variation using the PC for "up" and "down" magnetization states, we plotted the polarization states of the propagating light before, through, and after the PC using the Poincaré sphere for the hybrid device and the racetrack width of $w_{rt} = 120$ nm, where the target magnetic bit has DW = 200 nm. This specific value is chosen according to Fig. 4(b) in which the Kerr rotation magnitude is almost zero for the BW device. For this purpose, the Stokes parameters are defined by

$$S_1 = \cos 2\chi \cos 2\psi, \quad (1)$$

$$S_2 = \cos 2\chi \sin 2\psi, \quad (2)$$

$$S_3 = \sin 2\chi, \quad (3)$$

where ψ and χ are respectively the polarization rotation angle (Kerr rotation) and ellipticity angle (Kerr ellipticity), S_1 relates to the linearly polarized TM_0 and TE_0 components of light, S_2 indicates the orientation of linearly polarized modes at ±45°, and S_3 shows the light is whether left- or right-hand side circularly polarized light [70].

According to Fig. 5(b), while the propagating light has not yet entered the PC, the Stokes parameters on the Poincaré sphere indicate that $S_1 \approx 1$, and $S_{2,3} \approx 0$ upon changing the magnetization direction. According to these values, we can deduce that the propagating light has a dominant TE_0 component inside the waveguide before the PC, where changing the magnetization direction induces a phase difference between the TE_0 and PMOKE-induced TM_0 components of light. However, the PMOKE effect is so small that it cannot make a notable evolution in the polarization state of the incoming light. In contrast, when the light passes through the PC, the partial polarization conversion gives rise to the emergence of the TM_0 component with significant magnitude. Then both the TE_0 and TM_0 components beat together along the waveguide due to the waveguide's birefringence. This polarization conversion can be clearly seen in Fig. 5(c), where the polarization state of the propagating light evolves in the S_2-S_3 plane (i.e., $-1 \leq S_{2,3} \leq 1$). In sharp contrast to the previous case, we observe two slightly different values of S_1 for the "up" and "down" magnetization directions, respectively [see the blue and red curves in Fig. 5(c)]. This difference in the value of S_1 reflects the intensity variation in the TM_0 component of light originating from the PMOKE. In other words, the PMOKE-induced phase difference between the TE_0 and TM_0 components of the propagating light is translated into a PMOKE-induced variation in the intensity of the TM_0 component. Note that the spiral shape of the polarization evolution before and throughout the PC is because of the reflection from the gold metal layer back to the waveguide.

To provide memory readout based on the intensity variation of the generated TM_0 component, a figure of merit ΔS_1, representing the relative contrast, is defined as follows:

$$\Delta S_1(\%) = |S_{1,\uparrow} - S_{1,\downarrow}| \times 100, \quad (4)$$

where $S_{1,\uparrow}$ and $S_{1,\downarrow}$ are the output S_1 Stoke parameters defined by Eq. (1) for the upward and downward magnetization directions, respectively. Based on Eqs. (1) and (4), the relative contrasts for the BW and the PNA-PhC devices are 0.03% and 0.64%, respectively.

We can see that, using the bare waveguide, it is not possible to detect the difference in the state of a magnetic bit with a size beyond the diffraction limit. Conversely, our hybrid device curbed the diffraction limit challenge and identified the change in the magnetization direction in the same bit in the presence of oppositely magnetized background regions. It is worth mentioning that, as plotted in

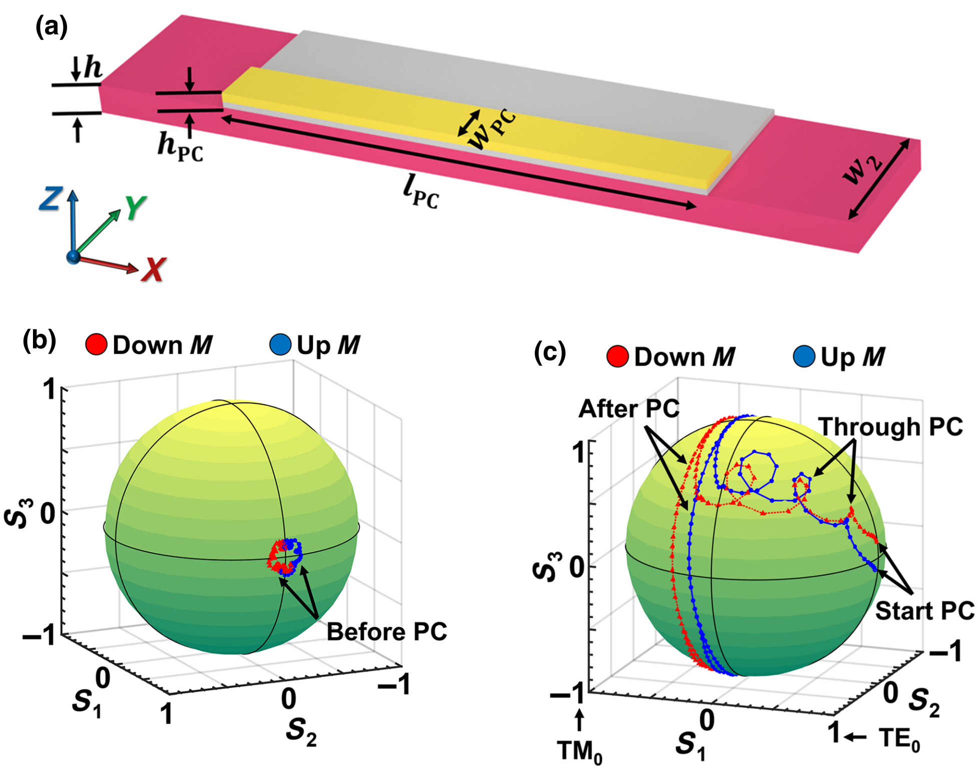

FIG. 5. Translation of a phase change to an intensity variation. (a) Schematic of the hybrid polarization converter (PC), where $w_2 = 440$ nm, $w_{PC} = 180$ nm, $h = 280$ nm, $h_{PC} = 50$ nm, and $l_{PC} = 1860$ nm are the widths of the InP waveguide and PC, the height of the waveguide and PC, and the length of the PC. (b),(c) Polarization state of light propagating through the waveguide using the Poincaré sphere: (b) before, (c) through, and after PC for a racetrack width of w_{rt} = 120 nm and the target magnetic bit with DW = 200 nm. Results for "up" (blue) and "down" (red) magnetization states are shown for an exaggerated value of MO efficiency for clarification.

Figs. 4(b) and 4(c), DW = 200 nm is not the smallest magnetic bit that can be read using the hybrid device. In fact, our proposed device can read magnetic bits with a footprint down to DW $\times$ $w_{rt}$$\sim$$100 \times 100$ nm^2 no matter what the magnetization state of the rest of the racetrack is, pointing towards the potential of our proposed hybrid device in enhancing MO effects at the nanoscale.

IV. DISCUSSION

Hybrid integration of spintronics and photonics has recently received growing interest. As for approaches to light projection onto spintronic devices, Becker *et al.* [71] proposed a two-dimensional grating coupler to project light pulses vertically into AOS-switchable magnetotunnel junctions (MTJs) [19,21,24]. Nevertheless, the large footprint and inefficient coupling curbed the further progress of this approach [23]. In addition, an extra requirement for interwafer integration imposes further challenges. In terms of multiplexing, Kimel and Li [9] proposed an integration scheme between AOS-switchable MTJs and photonic networks using cross-coupled photonic waveguides. In that work, the wavelength division multiplexing is based on arrays of Bragg gratings, which dictate the direction of wavelength-dependent outcoupling. However, such a multiplexing scheme of the light control comes with drawbacks of large footprint (diffraction limited to multiple of wavelength) and low coupling efficiency. In our proposed monolithic device, energy-efficient multiplexing is enabled by ultrafast domain wall motion [20] in a magnetic racetrack [39,40]. Moreover, the racetrack itself allows for ultradense data packing with a characteristic device size of $2F^2$ (where F defined as the characteristic minimum feature size in a given process technology) [40]. Our compact hybrid device further allows for photonic control of sub-100-nm spintronic devices, making our design an enabling technology for bridging integrated photonics with spintronics.

As to the photonic reading of nanostructured magnetic claddings on top of a photonic waveguide, our design provides a step beyond what has been reported by Demirer *et al.* [12,13]. Those papers demonstrated photonic reading of a *single, isolated magnetic cladding* with a size equal to the width of the waveguide. In contrast, we propose and analyze a design based on a PNA and a PhC that enables readout of *a selected domain out of a sequence of* *bits* in a magnetic racetrack that crosses the waveguide. Our simulations show that a resolution beyond the diffraction limit can be achieved, with bit sizes much smaller than the diameter of the waveguide. Furthermore, compared to the dielectric PC used in refs. [12,13]—needed for converting polarization to intensity modulation—our plasmonic PC may provide an advantage because of its ease of fabrication.

Our photonic reading scheme offers an alternative way of addressing magnetic information, compared to electronic readout by magnetoresistive effects, as exploited for instance in AOS-MTJs [19,21,24]. We argue that our approach allows us to encode the magnetic information directly in optical bit sequences in the photonic domain, without any intermediate electronic steps. This gives further room for energy-efficient, high-frequency, and tighter integration with photonic technologies.

V. CONCLUSION

In conclusion, we have designed an integrated hybrid plasmonic-photonic device capable of AOS and AOR of nanoscale ferrimagnet bits possessing PMA in a magnetic racetrack coupled onto an IMOS platform. The hybrid device consists of a double V-shaped PNA coupled with a PhC cavity. Enhanced, localized light offered by the strong light-mater interaction inside the cavity of the hybrid device proliferated the absorbed energy density and effective polarizability of a nanoscale target magnetic bit surrounded by oppositely magnetized background regions in a racetrack. Numerical results demonstrated that the absorbed energy density can be enhanced up to more than 30× (depending on the width of the magnetic racetrack from 120 nm down to 30 nm), exceeding the fluence threshold of switching in addition to preventing prevalent nonlinear absorption losses in the IMOS platform. Based on our numerical results, the hybrid device can enable the detection of the magnetization state in an approximately 200×100 nm^2 magnetic bit with a relative contrast greater than 0.6%, while target bits down to around 100×100 nm^2 can be identified distinctly, no matter what the magnetization state is in the background regions in the racetrack. All-optical access to a spintronic platform has turned into a hot topic in the field of spintronics, and we believe our proposed device can potentially bridge integrated photonics with spintronics for ultrafast and energy-efficient advanced on-chip applications.

ACKNOWLEDGMENTS

This work is part of the Gravitation program "Research Centre for Integrated Nanophotonics," which is financed by the Netherlands Organisation for Scientific Research (NWO). This project has also received funding from the European Union's Horizon 2020 research and innovation program under Marie Sklodowska-Curie Grant Agreement No. 860060.

H.P. and P.L. conceived and designed the project. H.P. carried out the designs, simulation of devices, and data analysis. P.L. performed the power/energy analysis for switching function. B.K. supervised the project. R.L., M.H., E.B., J.J.G.M.v.d.T, and B.K. contributed to the discussion and commented on the manuscript. H.P., P.L., and B.K. wrote the manuscript with input from all authors.

The authors declare no competing interests.

APPENDIX A: METHODS

1. Simulations of AOS and AOR

The numerical results of our studies in AOS and AOR are conducted using commercial Lumerical software [43]. The power absorption analysis was carried out using the *Power absorbed (advanced)* analysis group. To calculate the Kerr rotation due to PMOKE, we considered a multilayer stack of Ta(4)/Co(2)/Gd(4)/Pt(2), where the MO response is only considered for Co with a Voigt constant of $Q = 0.154 - 0.100i$ [72]. Knowing that Gd shows no MO response at optical wavelengths, the refractive index of Pt is used for Gd. To measure the Kerr rotation, we exploited the *Polarization ellipse* analysis group which returns the polarization rotation angle and ellipticity angle. Furthermore, a perfectly matched layer (PML) absorbing boundary condition is used to define the simulation domain. The refractive indices of all the materials in the simulations are selected from the material database of Lumerical [43]. Finally, for accurate numerical modeling of MO activity, a conformal mesh alongside an override mesh for the PNA and racetrack is defined with maximum mesh sizes of 5, 5, and 1 nm along the X, Y, and Z axes.

2. Pulse propagation with high intensity in passive waveguide

The traveling wave circuit model using the in-house PHIsim modeling software [56] with an extension of nonlinear effects is used to model the propagation of the fundamental TE_0 component of light in an InP waveguide on the IMOS platform. The nonlinear effects are introduced through modeling the evolution of the photon density (P), phase (ϕ), and its coupling to the charge density with the traveling distance and time:

$$\frac{dP_{1,2}}{dt} = (-\gamma_p - \gamma_{\text{car}} N) v_g P_{1,2} - 2\Gamma_2 \beta \hbar \omega v_g^2 (P_{1,2}^2 + P_1 P_2), \tag{A1}$$

$$\frac{d\phi_{1,2}}{dt} = \Gamma \alpha_p N - \Gamma_{2p} \frac{\beta \hbar \omega v_g n_2}{c} (P_1 + P_2), \tag{A2}$$

$$\frac{dN}{dt} = \frac{\Gamma_2 \beta \hbar \omega v_g^2}{\Gamma} (P_1^2 + P_2^2) - \frac{N}{\tau} - BN^2 - CN^3. \tag{A3}$$

The photon density as a signature of photon power of forward (P_1) and backward (P_2) propagation directions is modeled as Eq. (A1), where v_g is the group velocity, γ_p is the passive loss of the waveguide (80/m [49,73,74]), γ_{car} is the FCA coefficient (7.2×10^{-21}/m [49,51]), and β is the TPA coefficient (1.50×10^{-10} m/W [51]). The τ parameter is the carrier lifetime (2000 ps). The B and C parameters are the bimolecular recombination constant (2.62×10^{-16} m^3/s [75]) and Auger recombination constant (5.27×10^{-41} m^6/s [75]), respectively. The Γ_2 parameter is the two-photon confinement factor (0.7) as obtained from the Lumerical MODE solver [60]. The α_p parameter is the phase delay factor (1.7×10^{-26} m^3 [76]).

[1] W. Bogaerts, R. Baets, P. Dumon, V. Wiaux, S. Beckx, D. Taillaert, B. Luyssaert, J. Van Campenhout, P. Bienstman, and D. Van Thourhout, Nanophotonic waveguides in silicon-on-insulator fabricated with CMOS technology, J. Lightwave Technol. **23**, 401 (2005).

[2] W. Bogaerts, P. De Heyn, T. Van Vaerenbergh, K. De Vos, S. Kumar Selvaraja, T. Claes, P. Dumon, P. Bienstman, D. Van Thourhout, and R. Baets, Silicon microring resonators, Laser Photonics Rev. **6**, 47 (2012).

[3] J. J. van der Tol, Y. Jiao, J. P. Van Engelen, V. Pogoretskiy, A. A. Kashi, and K. Williams, InP membrane on silicon (IMOS) photonics, IEEE J. Quantum Electron. **56**, 1 (2019).

[4] Y. Jiao, J. van der Tol, V. Pogoretskii, J. van Engelen, A. A. Kashi, S. Reniers, Y. Wang, X. Zhao, W. Yao, T. Liu, *et al.*, Indium phosphide membrane nanophotonic integrated circuits on silicon, Phys. Status Solidi A **217**, 1900606 (2020).

[5] B. Dieny, I. L. Prejbeanu, K. Garello, P. Gambardella, P. Freitas, R. Lehndorff, W. Raberg, U. Ebels, S. O. Demokritov, J. Akerman, *et al.*, Opportunities and challenges for spintronics in the microelectronics industry, Nat. Electron. **3**, 446 (2020).

[6] S. Parkin and S.-H. Yang, Memory on the racetrack, Nat. Nanotechnol. **10**, 195 (2015).

[7] R. Bläsing, T. Ma, S.-H. Yang, C. Garg, F. K. Dejene, A. T. N'Diaye, G. Chen, K. Liu, and S. S. P. Parkin, Exchange coupling torque in ferrimagnetic Co/Gd bilayer maximized near angular momentum compensation temperature, Nat. Commun. **9**, 4984 (2018).

[8] P. Li, T. J. Kools, R. Lavrijsen, and B. Koopmans, Ultrafast racetrack based on compensated Co/Gd-based synthetic ferrimagnet with all-optical switching, Adv. Electron. Mater. **9**, 2200613 (2022).

[9] Alexey V. Kimel and M. Li, Writing magnetic memory with ultrashort light pulses, Nat. Rev. Mater. **4**, 189 (2019).

[10] N. Maccaferri, L. Bergamini, M. Pancaldi, M. K. Schmidt, M. Kataja, S. v. Dijken, N. Zabala, J. Aizpurua, and P. Vavassori, Anisotropic nanoantenna-based magnetoplasmonic crystals for highly enhanced and tunable magneto-optical activity, Nano Lett. **16**, 2533 (2016).

[11] F. Pineider and C. Sangregorio, in *Novel Magnetic Nanostructures* (Elsevier, Amsterdam, Netherlands, 2018), p. 191.

[12] F. E. Demirer, S. Reniers, R. Lavrijsen, B. Koopmans, and J. Van Der Tol, in *2021 Conference on Lasers and Electro-Optics Europe & European Quantum Electronics Conference (CLEO/Europe-EQEC)* (IEEE, Munich, Germany, 2021), p. 1.

[13] F. E. Demirer, Y. Baron, S. Reniers, D. Pustakhod, R. Lavrijsen, J. van der Tol, and B. Koopmans, An integrated photonic device for on-chip magneto-optical memory reading, Nanophotonics **11**, 3319 (2022).

[14] T. A. Ostler, *et al.*, Ultrafast heating as a sufficient stimulus for magnetization reversal in a ferrimagnet, Nat. Commun. **3**, 666 (2012).

[15] I. Radu, K. Vahaplar, C. Stamm, T. Kachel, N. Pontius, H. A. Dürr, T. A. Ostler, J. Barker, R. F. L. Evans, R. W. Chantrell, A. Tsukamoto, A. Itoh, A. Kirilyuk, T. Rasing, and A. V. Kimel, Transient ferromagnetic-like state mediating ultrafast reversal of antiferromagnetically coupled spins, Nature **472**, 205 (2011).

[16] C. D. Stanciu, F. Hansteen, A. V. Kimel, A. Kirilyuk, A. Tsukamoto, A. Itoh, and T. Rasing, All-Optical Magnetic Recording with Circularly Polarized Light, Phys. Rev. Lett. **99**, 047601 (2007).

[17] M. L. M. Lalieu, M. J. G. Peeters, S. R. R. Haenen, R. Lavrijsen, and B. Koopmans, Deterministic all-optical switching of synthetic ferrimagnets using single femtosecond laser pulses, Phys. Rev. B **96**, 220411 (2017).

[18] L. Avilés-Félix, L. Álvaro-Gómez, G. Li, C. S. Davies, A. Olivier, M. Rubio-Roy, S. Auffret, A. Kirilyuk, A. V. Kimel, T. Rasing, L. D. Buda-Prejbeanu, R. C. Sousa, B. Dieny, and I. L. Prejbeanu, Integration of Tb/Co multilayers within optically switchable perpendicular magnetic tunnel junctions, AIP Adv. **9**, 125328 (2019).

[19] L. Avilés-Félix, A. Olivier, G. Li, C. S. Davies, L. Álvaro-Gómez, M. Rubio-Roy, S. Auffret, A. Kirilyuk, A. V. Kimel, T. Rasing, L. D. Buda-Prejbeanu, R. C. Sousa, B. Dieny, and I. L. Prejbeanu, Single-shot all-optical switching of magnetization in Tb/Co multilayer-based electrodes, Sci. Rep. **10**, 5211 (2020).

[20] P. Li, M. J. G. Peeters, Y. L. W. van Hees, R. Lavrijsen, and B. Koopmans, Ultra-low energy threshold engineering for all-optical switching of magnetization in dielectric-coated Co/Gd based synthetic-ferrimagnet, Appl. Phys. Lett. **119**, 252402 (2021).

[21] L. Wang, C. Houyi, L. Pingzhi, L. Pingzhi, L. W. van Hees Youri, L. Yang, C. Kaihua, L. Reinoud, L. Xiaoyang, K. Bert, and Z. Weisheng, Picosecond optospintronic tunnel junctions, Proc. Natl. Acad. Sci. U.S.A. **119**, e2204732119 (2022).

[22] L. Wang, Y. L. W. van Hees, R. Lavrijsen, W. Zhao, and B. Koopmans, Enhanced all-optical switching and domain wall velocity in annealed synthetic-ferrimagnetic multilayers, Appl. Phys. Lett. **117**, 022408 (2020).

[23] E. K. Sobolewska, J. Pelloux-Prayer, H. Becker, G. Li, C. S. Davies, C. J. Krückel, L. A. Félix, A. Olivier, R. C. Sousa, I. L. Prejbeanu, A. I. Kiriliouk, D. V. Thourhout, T. Rasing, F. Moradi, and M. J. R. Heck, in *Proc. SPIE*, Vol. 11461 (California, United States, 2020).

[24] J.-Y. Chen, L. He, J.-P. Wang, and M. Li, All-Optical Switching of Magnetic Tunnel Junctions with Single Subpicosecond Laser Pulses, Phys. Rev. Appl. **7**, 021001 (2017).
[25] E. Hutter and J. H. Fendler, Exploitation of localized surface plasmon resonance, Adv. Mater. **16**, 1685 (2004).
[26] D. K. Gramotnev and S. I. Bozhevolnyi, Plasmonics beyond the diffraction limit, Nat. Photonics **4**, 83 (2010).
[27] H. Pezeshki, A. J. Wright, and E. C. Larkins, Ultra-compact and ultra-broadband hybrid plasmonic-photonic vertical coupler with high coupling efficiency, directivity, and polarisation extinction ratio, IET Optoelectron. **16**, 124 (2022).
[28] H. Pezeshki, Highly efficient, ultra-compact, and ultra-broadband bidirectional vertical coupler based on spin-directional locking, J. Opt. Soc. Am. B **39**, 2714 (2022).
[29] J. Mejía-Salazar and O. N. Oliveira Jr., Plasmonic biosensing: Focus review, Chem. Rev. **118**, 10617 (2018).
[30] H. Pezeshki, Ph.D. thesis, University of Nottingham, 2021.
[31] A. R. M. Zain, M. Gnan, H. M. Chong, M. Sorel, and M. Richard, Tapered photonic crystal microcavities embedded in photonic wire waveguides with large resonance quality-factor and high transmission, IEEE Photonics Technol. Lett. **20**, 6 (2007).
[32] H. Pezeshki and G. Darvish, Design of photonic crystal microcavity based optical switches using fano resonance effect, Optik **126**, 4202 (2015).
[33] S. F. Reniers, Y. Wang, K. A. Williams, J. J. Van Der Tol, and Y. Jiao, Characterization of waveguide photonic crystal reflectors on indium phosphide membranes, IEEE J. Quantum Electron. **55**, 1 (2019).
[34] E. Yablonovitch, Photonic crystals, J. Mod. Opt. **41**, 173 (1994).
[35] J. D. Joannopoulos, P. R. Villeneuve, and S. Fan, Photonic crystals: Putting a new twist on light, Nature **386**, 143 (1997).
[36] B. Ellis, M. A. Mayer, G. Shambat, T. Sarmiento, J. Harris, E. E. Haller, and J. Vučković, Ultralow-threshold electrically pumped quantum-dot photonic-crystal nanocavity laser, Nat. Photonics **5**, 297 (2011).
[37] H. Pezeshki and V. Ahmadi, All-optical bistable switching based on photonic crystal slab nanocavity using nonlinear Kerr effect, J. Mod. Opt. **60**, 103 (2013).
[38] H. Pezeshki and G. Darvish, Design and simulation of photonic crystal based all-optical logic gate and modulator using infiltration, Opt. Quantum Electron. **48**, 1 (2016).
[39] S. S. P. Parkin, M. Hayashi, and L. Thomas, Magnetic domain-wall racetrack memory, Science **320**, 190 (2008).
[40] R. Bläsing, A. A. Khan, P. C. Filippou, C. Garg, F. Hameed, J. Castrillon, and S. S. Parkin, Magnetic racetrack memory: From physics to the cusp of applications within a decade, Proc. IEEE **108**, 1303 (2020).
[41] I. M. Miron, K. Garello, G. Gaudin, P.-J. Zermatten, M. V. Costache, S. Auffret, S. Bandiera, B. Rodmacq, A. Schuhl, and P. Gambardella, Perpendicular switching of a single ferromagnetic layer induced by in-plane current injection, Nature **476**, 189 (2011).
[42] K.-S. Ryu, L. Thomas, S.-H. Yang, and S. Parkin, Chiral spin torque at magnetic domain walls, Nat. Nanotechnol. **8**, 527 (2013).
[43] FDTD, Lumerical Inc. (2022), https://www.lumerical.com/.
[44] A. Subramanian, P. Neutens, A. Dhakal, R. Jansen, T. Claes, X. Rottenberg, F. Peyskens, S. Selvaraja, P. Helin, B. Du Bois, *et al.*, Low-loss single mode PECVD silicon nitride photonic wire waveguides for 532–900 nm wavelength window fabricated within a CMOS pilot line, IEEE Photonics J. **5**, 2202809 (2013).
[45] J. H. Mentink, J. Hellsvik, D. V. Afanasiev, B. A. Ivanov, A. Kirilyuk, A. V. Kimel, O. Eriksson, M. I. Katsnelson, and T. Rasing, Ultrafast Spin Dynamics in Multisublattice Magnets, Phys. Rev. Lett. **108**, 057202 (2012).
[46] M. Beens, M. L. M. Lalieu, A. J. M. Deenen, R. A. Duine, and B. Koopmans, Comparing all-optical switching in synthetic-ferrimagnetic multilayers and alloys, Phys. Rev. B **100**, 220409 (2019).
[47] See the Supplemental Material at http://link.aps.org/supplemental/10.1103/PhysRevApplied.19.054036 for [give brief description of material]. All files related to a published paper are stored as a single deposit and assigned a supplemental material URL. This URL appears in the article's reference list. (2023).
[48] S. Gerlach, L. Oroszlany, D. Hinzke, S. Sievering, S. Wienholdt, L. Szunyogh, and U. Nowak, Modeling ultrafast all-optical switching in synthetic ferrimagnets, Phys. Rev. B **95**, 224435 (2017).
[49] S. Latkowski, V. Moskalenko, S. Tahvili, L. Augustin, M. Smit, K. Williams, and E. Bente, Monolithically integrated 2.5 GHz extended cavity mode-locked ring laser with intracavity phase modulators, Opt. Lett. **40**, 77 (2015).
[50] D. van Thourhout, C. R. Doerr, C. H. Joyner, and J. L. Pleumeekers, Observation of WDM crosstalk in passive semiconductor waveguides, IEEE Photonics Technol. Lett. **13**, 457 (2001).
[51] L. P. Gonzalez, J. M. Murray, S. Krishnamurthy, and S. Guha, Wavelength dependence of two photon and free carrier absorptions in InP, Opt. Express **17**, 8741 (2009).
[52] J. Gorchon, R. B. Wilson, Y. Yang, A. Pattabi, J. Y. Chen, L. He, J. P. Wang, M. Li, and J. Bokor, Role of electron and phonon temperatures in the helicity-independent all-optical switching of GdFeCo, Phys. Rev. B **94**, 184406 (2016).
[53] A. R. Khorsand, M. Savoini, A. Kirilyuk, A. V. Kimel, A. Tsukamoto, A. Itoh, and T. Rasing, Role of Magnetic Circular Dichroism in All-Optical Magnetic Recording, Phys. Rev. Lett. **108**, 127205 (2012).
[54] B. E. A. Saleh and M. C. Teich, *Fundamentals of Photonics* (Wiley, New York, United States, 2007).
[55] J. Wei, B. Zhang, M. Hehn, W. Zhang, G. Malinowski, Y. Xu, W. Zhao, and S. Mangin, All-Optical Helicity-Independent Switching State Diagram in Gd-Fe-Co Alloys, Phys. Rev. Appl. **15**, 054065 (2021).
[56] E. Bente, PHIsim—a photonic integrated circuit simulator (2021), https://sites.google.com/tue.nl/phisim/home.
[57] A. Gil-Molina, I. Aldaya, J. L. Pita, L. H. Gabrielli, H. L. Fragnito, and P. Dainese, Optical free-carrier generation in silicon nano-waveguides at 1550 nm, Appl. Phys. Lett. **112**, 251104 (2018).
[58] L. E. Black, A. Cavalli, M. A. Verheijen, J. E. M. Haverkort, E. P. A. M. Bakkers, and W. M. M. Kessels, Effective surface passivation of InP nanowires by atomic-layer-deposited Al_2O_3 with PO_x interlayer, Nano Lett. **17**, 6287 (2017).

[59] E. Bente, S. Andreou, Y. Jiao, and K. Williams, in *2021 Conference on Lasers and Electro-Optics Europe & European Quantum Electronics Conference (CLEO/Europe-EQEC)* (IEEE, Munich, Germany, 2021), p. 1.

[60] MODE, Lumerical Inc. (2022), https://www.lumerical.com/.

[61] M. Kataja, T. Hakala, A. Julku, M. Huttunen, S. van Dijken, and P. Törmä, Surface lattice resonances and magneto-optical response in magnetic nanoparticle arrays, Nat. Commun. **6**, 1 (2015).

[62] V. G. Kravets, A. V. Kabashin, W. L. Barnes, and A. N. Grigorenko, Plasmonic surface lattice resonances: A review of properties and applications, Chem. Rev. **118**, 5912 (2018).

[63] P. B. Johnson and R.-W. Christy, Optical constants of the noble metals, Phys. Rev. B **6**, 4370 (1972).

[64] P. Li, J. W. van der Jagt, M. Beens, J. Hintermayr, M. Verheijen, R. Bruikman, B. Barcones, R. Juge, R. Lavrijsen, D. Ravelosona, and B. Koopmans, Enhancing all-optical switching of magnetization by He ion irradiation, Appl. Phys. Lett. **121**, 172404 (2022).

[65] K. Garello, F. Yasin, H. Hody, S. Couet, L. Souriau, S. H. Sharifi, J. Swerts, R. Carpenter, S. Rao, W. Kim, J. Wu, K. K. V. Sethu, M. Pak, N. Jossart, D. Crotti, A. Furnémont, and G. S. Kar, in *2019 Symposium on VLSI Circuits* (2019), p. T194.

[66] H. Pezeshki, Ultra-compact and-broadband integrated plasmonic waveplates with high efficiency, Appl. Phys. B **128**, 1 (2022).

[67] H. Deng, D. O. Yevick, C. Brooks, and P. E. Jessop, Design rules for slanted-angle polarization rotators, J. Lightwave Technol. **23**, 432 (2005).

[68] L. Gao, Y. Huo, J. S. Harris, and Z. Zhou, Ultra-compact and low-loss polarization rotator based on asymmetric hybrid plasmonic waveguide, IEEE Photonics Technol. Lett. **25**, 2081 (2013).

[69] H. Pezeshki, P. Li, R. Lavrijsen, J. J. G. M. Van Der Tol, and B. Koopmans, Optical reading of nanoscale magnetic bits in an integrated photonic platform, IEEE J. Quantum Electron. **25**, 1 (2022).

[70] E. Collett, *Field Guide to Polarization* (SPIE Bellingham, WA, 2005).

[71] H. Becker, C. J. Krückel, D. V. Thourhout, and M. J. R. Heck, Out-of-plane focusing grating couplers for silicon photonics integration with optical MRAM technology, IEEE J. Sel. Top. Quantum Electron. **26**, 1 (2020).

[72] W. Van Parys, Ph.D. thesis, Ghent University, 2009.

[73] L. M. Augustin, R. Santos, E. den Haan, S. Kleijn, P. J. A. Thijs, S. Latkowski, D. Zhao, W. Yao, J. Bolk, H. Ambrosius, S. Mingaleev, A. Richter, A. Bakker, and T. Korthorst, InP-based generic foundry platform for photonic integrated circuits, IEEE J. Sel. Top. Quantum Electron. **24**, 1 (2018).

[74] M. Smit, K. Williams, and J. van der Tol, Past present, and future of InP-based photonic integration, APL Photonics **4**, 050901 (2019).

[75] E. A. J. M. Bente, Y. Barbarin, M. J. R. Heck, and M. K. Smit, Modeling of integrated extended cavity InP/InGaAsP semiconductor modelocked ring lasers, Opt. Quantum Electron. **40**, 131 (2008).

[76] M. D. Dvorak, B. L. Justus, D. K. Gaskill, and D. G. Hendershot, Nonlinear absorption and refraction of quantum confined InP nanocrystals grown in porous glass, Appl. Phys. Lett. **66**, 804 (1995).